INTERNATIONAL JOURNAL FOR NUMERICAL METHODS IN FLUIDS, VOL. 25, 615–631 (1997)

DEVELOPMENT OF A MULTIBLOCK PRESSURE-BASED ALGORITHM USING MIXED INTERPOLATION FOR TURBULENT FLOWS

D. L. HILL[1,2]* AND E. A. BASKHARONE[1]

[1] *Department of Mechanical Engineering, Texas A&M University, College Station, TX 77843-3123, U.S.A.*
[2] *Lenexa Products, Lenexa, KS 66215, U.S.A.*

SUMMARY

A new multiblock pressure-based finite element algorithm has been developed. This methodology implements a novel quadratic interpolation for the elemental pressure while using a bilinear interpolation for the velocity. Details of the algorithm and its multiblock foundation are provided along with a complete description of the implementation of the RNG-based k–ε model. The results presented clearly demonstrate the validity and accuracy of this new approach for complex flow problems such as diffusers. © 1997 John Wiley & Sons, Ltd.

Int. J. Numer. Meth. Fluids, **25**: 615–631 (1997)

No. of Figures: 12. No. of Tables: 1. No. of References: 23.

KEY WORDS: finite elements; multiblock; mixed order; turbulence

1. INTRODUCTION

Primitive variable finite element algorithms have been traditionally developed under the assumption that the pressure interpolating function must be at a lower order than the velocity variables. This may be true for non-staggered methods that must satisfy the Brabuska–Brezzi[1] compatibility conditions, but not for the newer algorithms that parallel the SIMPLE-type[2] approach. The works of Rice and Schnipke,[3] Shaw[4] and Comini and Del Giudice[5] develop different algorithms that use equal-order interpolation for the flow variables. None of the solutions presented indicated any signs of the decoupling 'checkerboard' problem that normally occurs with pressure. The algorithm in the current work uses a novel approach of interpolating the pressure quadratically and the velocity field bilinearly. The higher-order interpolation has been found to increase both the stability and convergence rate of the Laplacian-type pressure equation used in the algorithm. The choice of using the higher-order interpolation for pressure was also influenced by the authors' unpublished work that used a linear approximation for the elemental pressure field. In this work the pressure distribution was found to oscillate and had to be heavily underrelaxed. This effort as well as the current study uses the algorithm based on the SIMPLER approach reported by Rice and Schnipke.[3] The current study also

---

* Correspondence to: D. L. Hill, Department of Mechanical Engineering, Texas A&M University, College Station, TX 77843-3123, U.S.A.

CCC 0271–2091/97/060615–17 $17.50

Received 22 September 1995
Revised 27 September 1996

uses the multiblock scheme reported by Hill and Baskharone[6] with changes made for turbulent problems.

Turbulence is modelled using an RNG-based high-Reynolds-number (*Re*) model developed by Yakhot *et al.*[7,8] The approach used to implement the RNG model was derived from the reported finite element formulations of the standard high-*Re* k–ε model. The primary differences between these two models are the constants and the source term in the dissipation rate equation. There are some variations in the techniques used to split or linearize source terms, but the main differences in the algorithms reviewed were with the manner in which the wall functions were imposed. This region is of prime concern for problems involving wall-generated turbulence.

The work of Thomas *et al.*[9] was one of the pioneering efforts which imposed the velocity using the wall functions. Their approach displaced the near-wall elements by a small distance away from the boundary. This small region was essentially removed from the computational domain and allowed the wall functions to be applied to the boundary nodes that previously fell on the solid boundaries. This recursive approach uses the most recent discrete values of velocity to calculate a normal derivative for velocity. This value is used to approximate the wall shear stress. Using the new wall stress and the wall functions gives rise to the new tangential velocity. The normal velocity, however, was set to zero. The functions that relate k and ε to the wall stress were derived from the near-wall assumption that turbulence production equals dissipation.

An improvement to this wall function approach was reported by Benim and Zinser.[10] This work, which was based-on quadrilateral elements, was derived using a two-point stencil. At what would be the farthest point from the wall, the shear stress was calculated. This value was obtained using the most recent tangential velocity at that node in conjunction with the relation for the turbulence parameter y^+ suggested by Launder and Spalding.[11] This relation requires the turbulent kinetic energy, which in turn is taken from the near-wall node in the stencil. Assuming that both nodes fall on the same logarithmic curve, the new shear stress was directly used in the wall functions to calculate a new value of the tangential velocity for the near-wall node in the stencil. Instead of specifying a zero normal velocity, a novel mass balance technique was used by these authors to resolve this value. This approach was extended to general non-orthogonal domains by computing, not specifying, the point location farthest away from the wall in the two-point stencil.[12] This method projects a normal line from the wall through the first point and terminates it when it intersects the wall of the element located on the second layer of elements from the wall.

A method for imposing the wall shear stress was reported by Schnipke.[13] This work parallels the approach commonly employed in finite volume codes such as TEACH-2E[14] and KIVA-II.[15] At near-wall nodes the relation proposed by Launder and Spalding[11] is also used to obtain the required y^+-value. By manipulating the wall function relations, the y^+-value is used to calculate a new value of turbulent viscosity. Using this value and the known form of the normal derivative for velocity, the new shear stress was formed. Imposing the same turbulent viscosity at both the wall and the near-wall node resulted in a constant shear stress approximation for the momentum equations. The shear stress was also modified in the generation term of the turbulent kinetic energy equation for elements adjacent to solid walls. The expression by Pun and Spalding[16] was used for the boundary condition of ε at all near-wall nodes.

The method adopted in the current algorithm has integrated the concepts from both methods to arrive at a unique finite element implementation of the standard wall functions. This approach, along with the finite element equations, is developed in the next section. The results of the validation effort for the algorithm with the RNG-based high-*Re* model are then reported. The study performed is considered a ‘worst’-case scenario for the model and the results are compared both with experimental data and with numerical solutions using the standard high-*Re* k–ε model. Conclusions drawn from this study are given in the final section.

2. ANALYSIS

The finite element equations developed in this section are formulated under the assumption that the fluid flow is Newtonian, steady, axisymmetric and incompressible. The Reynolds-averaged flow governing equations for this class of flow problem are as follows,

continuity

$$\frac{1}{r}\frac{\partial}{\partial r}(rv)+\frac{1}{r}\frac{\partial}{\partial x}(ru)=0, \tag{1a}$$

radial momentum

$$\rho v\frac{\partial v}{\partial r}+\rho u\frac{\partial v}{\partial x}=-\frac{\partial p}{\partial r}+\frac{1}{r}\left[\frac{\partial}{\partial r}\left(r\mu_{\mathrm{e}}\frac{\partial v}{\partial r}\right)+\frac{\partial}{\partial x}\left(r\mu_{\mathrm{e}}\frac{\partial v}{\partial x}\right)\right]-\frac{\mu_{\mathrm{e}}v}{r^2}, \tag{1b}$$

axial momentum

$$\rho v\frac{\partial u}{r}+\rho u\frac{\partial u}{\partial x}=-\frac{\partial p}{\partial x}+\frac{1}{r}\left[\frac{\partial}{\partial r}\left(r\mu_{\mathrm{e}}\frac{\partial u}{\partial r}\right)+\frac{\partial}{\partial x}\left(r\mu_{\mathrm{e}}\frac{\partial u}{\partial x}\right)\right], \tag{1c}$$

where v, u, p and ρ are the Reynolds-averaged values of the velocity components, pressure and density respectively and μ_{e} is the effective viscosity defined as $\mu_{\mathrm{e}}=\mu+\mu_{\mathrm{t}}$. Use of the two-equation model dictates that μ_{t} be defined in terms of both the kinetic energy and the dissipation rate as follows,

$$\mu_{\mathrm{t}}=\rho C_{\mu}\frac{k^2}{\varepsilon}, \tag{2}$$

where k is the Reynolds-averaged turbulent kinetic energy, ε is the Reynolds-averaged dissipation rate and C_{μ} is a constant. The transport equations used to calculate the turbulence quantities for equation (2) are provided from the RNG-based high-*Re* k–ε model and are given in their axisymmetric form as follows:

turbulent kinetic energy

$$\rho v\frac{\partial k}{\partial r}+\rho u\frac{\partial k}{\partial x}=\frac{1}{r}\left[\frac{\partial}{\partial r}\left(r\frac{\mu_{\mathrm{e}}}{\sigma_k}\frac{\partial k}{\partial r}\right)+\frac{\partial}{\partial x}\left(r\frac{\mu_{\mathrm{e}}}{\sigma_k}\frac{\partial k}{\partial x}\right)\right]=\mu_{\mathrm{t}}G_k-\rho\varepsilon, \tag{3a}$$

where

$$G_k=2\left[\left(\frac{\partial u}{\partial x}\right)^2+\left(\frac{\partial v}{\partial r}\right)^2+\left(\frac{v}{r}\right)^2\right]+\left(\frac{\partial u}{\partial r}+\frac{\partial v}{\partial x}\right)^2, \tag{3b}$$

dissipation rate

$$\rho v\frac{\partial \varepsilon}{\partial r}+\rho u\frac{\partial \varepsilon}{\partial x}=\frac{1}{r}\left[\frac{\partial}{\partial r}\left(r\frac{\mu_{\mathrm{e}}}{\sigma_{\varepsilon}}\frac{\partial \varepsilon}{\partial r}\right)+\frac{\partial}{\partial x}\left(r\frac{\mu_{\mathrm{e}}}{\sigma_{\varepsilon}}\frac{\partial \varepsilon}{\partial x}\right)\right]=\frac{C_1\mu_{\mathrm{t}}\varepsilon}{k}G_k-\frac{C_2\rho\varepsilon^2}{k}-R, \tag{3c}$$

where

$$R=\frac{v_{\mathrm{t}}S^3}{1+0{\cdot}012\eta^3}\left(1-\frac{\eta}{4{\cdot}38}\right), \tag{3d}$$

$$\eta=\frac{Sk}{\varepsilon},\qquad S=\surd G_k. \tag{3e}$$

Table I. Comparison of constants for different k–ε models

	C_μ	σ_k	σ_ε	C_1	C_2	κ
Standard k–ε model	0·09	1·0	1·0	1·44	1·92	0·4
RNG-based, k–ε model	0·09	1·39	1·39	1·42	1·68	0·4

In equations (3a–c), C_1, C_2, C_μ, σ_k and σ_ε are constants that differ from those used in the standard high-*Re* k–ε model. A comparison between these two sets of constants is given in Table I.

Equations (1a–c), (2) and (3a–e) comprise the set of flow governing equations. Development of the finite element form of these equations is performed using their non-dimensional form. The following expressions are used in the non-dimensionalization process:

$$\begin{gathered} u^* = u/U, \qquad v^* = v/U, \qquad p^* = (p - P)/\rho U^2, \\ x^* = x/L, \qquad r^* = r/L, \qquad \mu^* = \mu_1/\mu, \\ k^* = k/U^2, \qquad \varepsilon^* = \varepsilon L/U^3, \end{gathered} \tag{4}$$

where U, L, P and μ are the reference values for velocity, length, pressure and viscosity respectively. The final non-dimensional form of the flow governing equations is given as follows:

continuity

$$\frac{1}{r^*}\frac{\partial}{\partial r^*}(r^* v^*) + \frac{1}{r^*}\frac{\partial}{\partial x^*}(r^* u^*) = 0, \tag{5a}$$

radial momentum

$$v^*\frac{\partial v^*}{\partial r^*} + u^*\frac{\partial v^*}{\partial x^*} = \frac{1}{Re}\frac{1}{r^*}\left[\frac{\partial}{\partial r^*}\left(r^*\mu^*_{\mathrm{lt}}\frac{\partial v^*}{\partial r^*}\right) + \frac{\partial}{\partial x^*}\left(r^*\mu_{\mathrm{lt}}\frac{\partial v^*}{\partial x^*}\right)\right] - \frac{\partial p^*}{\partial r^*} - \frac{\mu^*_{\mathrm{lt}}}{Re}\frac{v^*}{r^{*2}}, \tag{5b}$$

axial momentum

$$v^*\frac{\partial u}{\partial r^*} + u^*\frac{\partial u^*}{\partial x^*} = \frac{1}{Re}\frac{1}{r^*}\left[\frac{\partial}{\partial r^*}\left(r^*\mu^*_{\mathrm{lt}}\frac{\partial u^*}{\partial r^*}\right) + \frac{\partial}{\partial x^*}\left(r^*\mu^*_{\mathrm{lt}}\frac{\partial u^*}{\partial x^*}\right)\right] - \frac{\partial p^*}{\partial x^*}, \tag{5c}$$

k-equation

$$v^*\frac{\partial k^*}{\partial r^*} + u^*\frac{\partial k^*}{\partial x^*} = \frac{1}{Re}\frac{1}{r^*}\left[\frac{\partial}{\partial r^*}\left(r^*\frac{\mu^*_{\mathrm{lt}}}{\sigma_k}\frac{\partial k^*}{\partial r^*}\right) + \frac{\partial}{\partial x^*}\left(r^*\frac{\mu^*_{\mathrm{lt}}}{\sigma_k}\frac{\partial k^*}{\partial x^*}\right)\right] + \mu^* G^*_k - \varepsilon^*, \tag{5d}$$

ε-equation

$$v^*\frac{\partial \varepsilon^*}{\partial r^*} + u^*\frac{\partial \varepsilon^*}{\partial x^*} = \frac{1}{Re}\frac{1}{r^*}\left[\frac{\partial}{\partial r^*}\left(r^*\frac{\mu^*_{\mathrm{lt}}}{\sigma_k}\frac{\partial \varepsilon^*}{\partial r^*}\right) + \frac{\partial}{\partial x^*}\left(r^*\frac{\mu^*_{\mathrm{lt}}}{\sigma_k}\frac{\partial \varepsilon^*}{\partial x^*}\right)\right] + \frac{C_1\mu^*\varepsilon^*}{k^*}G^*_k - \frac{C_2\varepsilon^{*2}}{k^*} - R^*, \tag{5e}$$

where the following relations are now defined:

$$G^*_k = 2\left[\left(\frac{\partial u^*}{\partial x^*}\right)^2 + \left(\frac{\partial v^*}{\partial r^*}\right)^2 + \left(\frac{v^*}{r^*}\right)^2\right] + \left(\frac{\partial u^*}{\partial r^*} + \frac{\partial v^*}{\partial x^*}\right)^2, \tag{5f}$$

$$R^* = \frac{\mu^* S^{*3}}{1 + 0{\cdot}012\eta^{*3}}\left(1 - \frac{\eta^*}{4{\cdot}38}\right), \qquad \eta^* = \frac{S^* k^*}{\varepsilon^*}, \qquad S^* = \surd G^*_k, \tag{5g}$$

$$\mu^* = \frac{\mu_{\mathrm{t}}}{\mu} = \frac{C_\mu Re k^{*2}}{\varepsilon^*}, \qquad \mu^*_{\mathrm{lt}} = 1 + \mu^*. \tag{5h}$$

The finite element formulation follows the same logic that was reported by Hill and Baskharone,[6] except that two additional equations are now solved after the velocity has been corrected and the flow field is axisymmetric. The minor changes in the finite element equations prior to this point in the computational loop are found in the intermediate velocity equations where the effective viscosity now varies. These changes have been incorporated and the superscript asterisks dropped for simplification to produce the resulting equations as follows:

radial momentum

$$\begin{aligned}\left[\int \tilde{W}_i\left(\bar{v}\frac{\partial M_j}{\partial r}+\bar{u}\frac{\partial M_j}{\partial x}\right)\mathrm{d}A^{\mathrm{e}}+\frac{\overline{\mu_{\mathrm{el}}}}{Re\,\bar{r}}\int\left(\frac{\partial W_i}{\partial r}\frac{\partial M_j}{\partial r}+\frac{\partial W_i}{\partial x}\frac{\partial M_j}{\partial x}\right)\mathrm{d}A^{\mathrm{e}}\right]v_j \\ =-\int \tilde{W}_i\frac{\partial N_i}{\partial r}p_j\,\mathrm{d}A^{\mathrm{e}}-\frac{\overline{\mu_{\mathrm{lt}}}\bar{v}}{Re\,\bar{r}^2}+\frac{1}{Re}\int \tilde{W}_i(\bar{r}\nabla v\cdot n)\,\mathrm{d}l,\end{aligned} \tag{6a}$$

axial momentum

$$\begin{aligned}\left[\int \tilde{W}_i\left(\bar{v}\frac{\partial M_j}{\partial r}+\bar{u}\frac{\partial M_j}{\partial x}\right)\mathrm{d}A^{\mathrm{e}}+\frac{\overline{\mu_{\mathrm{tl}}}}{Re\,\bar{r}}\int\left(\frac{\partial W_i}{\partial r}\frac{\partial M_j}{\partial r}+\frac{\partial W_i}{\partial x}\frac{\partial M_j}{\partial x}\right)\mathrm{d}A^{\mathrm{e}}\right]u_j \\ =-\int \tilde{W}_i\frac{\partial N_i}{\partial r}p_j\,\mathrm{d}A^{\mathrm{e}}+\frac{1}{Re}\int \tilde{W}_i(\bar{r}\nabla u\cdot n)\,\mathrm{d}l,\end{aligned} \tag{6b}$$

where $\mathrm{d}A^{\mathrm{e}}$ is the differential axisymmetric area ($r\,\mathrm{d}r\,\mathrm{d}z$), M_i is the bilinear shape function and N_j is the quadratic shape function. $\tilde{W}_i$ is a weighting function with a perturbation function component added ($\tilde{W}_i = W_i + \tilde{P}_i$). The perturbation function is a result of the upwind scheme and its value is obtained on an element basis using the local velocity field. This upwinding technique was first reported by Brooks and Hughes[17] and has been proven to be less diffusive than the streamline upwind method developed by Rice and Schnipke.[18] The weighting function W_i for these equations is bilinear. All variables with overbars are interpolated at integration points using the most recent values of the indicated variables.

The pressure and velocity correction equations remain nearly unchanged except for the minor axisymmetric modifications and are given as follows for completeness:

pressure equation

$$\int\left(\overline{K_v}\frac{\partial N_i}{\partial r}\frac{\partial N_j}{\partial r}+\overline{K_u}\frac{\partial N_i}{\partial x}\frac{\partial N_j}{\partial x}\right)p_j\,\mathrm{d}A^{\mathrm{e}}=\int\frac{\partial N_i}{\partial x}(M_k\hat{u}_k)+\frac{\partial N_i}{\partial r}(M_k\hat{v}_k)\,\mathrm{d}A^{\mathrm{e}}+\int N_i(V\cdot n)\,\mathrm{d}l, \tag{7}$$

velocity correction

$$v_i=\hat{v}_i+\frac{1}{a_{ii}}\sum_{j=1,m}b^v_{ij}p_j,\qquad u_i=\hat{u}_i+\frac{1}{a_{ii}}\sum_{j=1,m}b^u_{ij}p_j. \tag{8}$$

For equations (7) and (8) the 'hatted' velocities are the sum of the off-diagonal coefficients of the momentum equations multiplied by the nodal intermediate velocity values. After these nodal quantities are computed, the velocity update is performed using the new pressure field. Next, the solution of the turbulent kinetic energy and dissipation rate is carried out. The finite element form of these equations, which was used in this work, was developed using equation (5h) to obtain forms of the source terms that can be linearized in terms of the field variable being solved. This splitting technique can be written as follows:

$$S^n=S^{n-1}+\frac{\partial S}{\partial\phi}(\phi^{n-1})(\phi^n-\phi^{n-1}). \tag{9}$$

The dissipation source term in equation (5d) for the turbulent kinetic energy is manipulated using this procedure. The intermediate results for this term are given first, followed by the elemental turbulent kinetic energy equation:

$$\varepsilon = \frac{C_\mu\ Re\ k^2}{\mu}, \qquad \varepsilon = \frac{C_m u\ Re\ k_{\text{old}}^2}{\mu} + \frac{2C_\mu\ Re\ k_{\text{old}}}{\mu}(k - k_{\text{old}}), \qquad \varepsilon = \frac{C_\mu\ Re\ k_{\text{old}}^2}{\mu} + \frac{C_\mu\ Re\ k_{\text{old}} k}{\mu},$$

k-equation

$$\left[\int \tilde{W}_i\left(\bar{v}\frac{\partial M_j}{\partial r} + \bar{u}\frac{\partial M_j}{\partial x}\right)\mathrm{d}A^{\mathrm{e}} + \frac{\overline{\mu_{\text{tl}}}/\sigma_k}{Re\ \bar{r}}\int\left(\frac{\partial W_i}{\partial r}\frac{\partial M_j}{\partial r} + \frac{\partial W_i}{\partial x}\frac{\partial M_j}{\partial x}\right)\mathrm{d}A^{\mathrm{e}} + \int W_i\frac{2C_\mu\ Re\ \bar{k}M_j}{\bar{\mu}}\mathrm{d}A^{\mathrm{e}}\right]k_j$$
$$= \int \tilde{W}_i\left(\bar{G}_k + \frac{C_\mu\ Re\ \bar{k}^2}{\bar{\mu}}\right)\mathrm{d}A^{\mathrm{e}} + \frac{1}{Re}\int \tilde{W}_i(\bar{r}\nabla k\cdot n)\,\mathrm{d}l. \tag{10}$$

Two of the source terms in the ε-equation are now developed. The first source, on the right side of equation (5e), is modified by inserting equation (5h). This step results in the following expression for this source term:

$$\frac{C_1\mu\varepsilon}{k}G_k = C_1 C_\mu\ Re\ kG_k.$$

Next, the linearizing technique expressed by equation (9) is applied to the second source term on the right side of equation (5e), giving rise to the following results:

$$\frac{C_2\varepsilon^2}{k} = \frac{C_\mu\varepsilon_{\text{old}}^2}{k} + \frac{2C_\mu\varepsilon_{\text{old}}}{k}(\varepsilon - \varepsilon_{\text{old}}), \qquad \frac{C_2\varepsilon^2}{k} = \frac{C_\mu\varepsilon_{\text{old}}^2}{k} + \frac{C_\mu\varepsilon_{\text{old}}\varepsilon}{k}.$$

These two new expressions are used in equation (5e) to produce the final form of the ε-equation as follows,

ε-equation

$$\left[\int \tilde{W}_i\left(\bar{v}\frac{\partial M_j}{\partial r} + \bar{u}\frac{\partial M_j}{\partial x}\right)\mathrm{d}A^{\mathrm{e}} + \frac{\overline{\mu_{\text{tl}}}/\sigma_\varepsilon}{Re\ \bar{r}}\int\left(\frac{\partial Wi}{\partial r}\frac{\partial M_j}{\partial r} + \frac{\partial W_i}{\partial x}\frac{\partial M_j}{\partial x}\right)\mathrm{d}A^{\mathrm{e}} + \int W_i\frac{2C_\mu\bar{\varepsilon}M_j}{\bar{k}}\mathrm{d}A^{\mathrm{e}}\right]\varepsilon_j$$
$$= \int \tilde{W}_i\left(C_1 C_\mu Re\ \overline{kG_k} + \frac{C_2\bar{\varepsilon}^2}{\bar{k}} - \bar{R}\right)\mathrm{d}A^{\mathrm{e}} + \frac{1}{Re}\int \tilde{W}_i(\bar{r}\nabla\varepsilon\cdot n)\,\mathrm{d}l. \tag{11}$$

The system of equations given by (6a,b), (7), (8), (10) and (11) represents the finite element equations for a single block and is supplemented by equations (5g,h) and Table I. Implementation of these equations into the multiblock format, for inner-block boundary nodes, follows the same approach as developed by Hill and Baskharone.[6] The discretized form is used to emphasize the contributions obtained from a foreign block. The final form of this set of equations is given as follows:

radial momentum

$$(a_{ii} + a'_{ii})v_i + \sum_{j=1,m}^{i\neq j}(a_{ij} + a'_{ij})v_j = \sum_{j=1,n}(b^v_{ij} + b^{v'}_{ij})p_j + s^v_i, \tag{12a}$$

axial momentum

$$(a_{ii} + a'_{ii})u_i + \sum_{j=1,m}^{i\neq j}(a_{ij} + a'_{ij})u_j = \sum_{j=1,n}(b^u_{ij} + b^{u'}_{ij})p_j + s^u_i, \tag{12b}$$

where

$$s_i^v = (r_i^v + r_i^{v'}) + \sum_{j=1,k} b_{ij}^{v'} p_j' - \sum_{j=1,l} a_{ij}' v_j', \qquad s_i^u = \sum_{j=1,k} b_{ij}^{u'} p_j' - \sum_{j=1,l} a_{ij}' u_j'.$$

The superscript primes denote contributions from a foreign block and r_i^v represents the source term in the radial momentum equation. Note that the limits in the summation expressions for the pressure and velocity are now different. The pressure equation and the velocity correction are given as follows:

pressure equation

$$(c_{ii} + c_{ii}')p_i = \sum_{j=1,n}^{i\neq j} (c_{ij} + c_{ij}')p_j = (d_i - d_i') - \sum_{j=1,k} c_{ij}' p_j', \tag{12c}$$

velocity correction

$$v_i = \hat{v}_i - \sum_{j=1,n} (b_{ij}^v + b_{ij}^{v'})p_j - \sum_{j=1,k} b_{ij}^{v'} p_j', \qquad u_i = \hat{u}_i - \sum_{j=1,n} (b_{ij}^u + b_{ij}^{u'})p_j - \sum_{j=1,k} b_{ij}^{u'} p_j'. \tag{12d}$$

For consistency the expressions for $\hat{u}$ and $\hat{v}$ are updated and presented as follows:

$$\hat{v}_i = -\sum_{j=1,m}^{i\neq j} (a_{ij} + a_{ij}')v_j - \sum_{j=1,l} a_{ij}' v_j', \qquad \tilde{u}_i = -\sum_{j=1,m}^{i\neq j} (a_{ij} + a_{ij}')u_j - \sum_{j=1,l} a_{ij}' u_j'.$$

The form of the multiblock expressions for k and ε can now be derived from equation (12a) as follows:

k-equation

$$(a_{ii} + a_{ii}')k_i + \sum_{j=1,m}^{i\neq j} (a_{ij} + a_{ij}')k_j = s_i^k, \tag{12e}$$

ε-equation

$$(a_{ii} + a_{ii}')\varepsilon_i + \sum_{j=1,m}^{i\neq j} (a_{ij} + a_{ij}')\varepsilon_j = s_i^\varepsilon, \tag{12f}$$

where

$$s_i^k = (r_i^k + r_i^{k'}) - \sum_{j=1,l} a_{ij}' k_j', \qquad s_i^\varepsilon = (r_i^\varepsilon + r_i^{\varepsilon'}) - \sum_{j=1,l} a_{ij}' \varepsilon_j'.$$

The selected approach for implementing wall functions utilizes the constant wall shear stress characteristic of these functions. The law of the wall and log law of the wall are described in Reference 19 and are given as follows:

law of the wall

$$u_{\mathrm{t}} = \frac{y_{\mathrm{n}} \tau_{\mathrm{w}}}{\mu} \tag{13a}$$

log law of the wall

$$\frac{u_{\mathrm{t}}}{\sqrt{(\tau_{\mathrm{w}}/\rho)}} = \frac{1}{\kappa} \ln\left(\frac{y_{\mathrm{n}} \sqrt{(\tau_{\mathrm{w}}/\rho)}}{\nu}\right) + B, \tag{13b}$$

where u_t, y_n and τ_w are the tangential velocity, the normal distance to the solid boundary and the wall shear stress respectively. B and κ are constants and have the approximate values 5·5 and 0·41 respectively. Accordingly, the definition of y^+ is given as follows:

$$y^+ = \frac{y_n}{\nu}\sqrt{\left(\frac{\tau_w}{\rho}\right)}. \tag{14}$$

For the condition $y^+ \leqslant 12$ the law of the wall is used to represent the wall shear stress as follows:

$$\tau_w = \mu\frac{u_t}{y_n}. \tag{15}$$

For the condition $y^+ > 12$, equation (13b) can be minipulated using equation (14) to derive an equivalent form for the shear stress as follows:

$$\tau_w = \mu\frac{\kappa y^+}{\ln(Ey^+)}\frac{u_t}{u_n} \tag{16}$$

where E is defined as the inverse log of $B\kappa$. The value of viscosity for the near-wall region can be derived form equations (15) and (16). For $y^+ \leqslant 12$ the near-wall value of viscosity will be the laminar value. For $y^+ > 12$, equation (16) implies that the required turbulent viscosity will have the form:

$$\mu_w = \mu\frac{\kappa y^+}{\ln(Ey^+)}.$$

The computational sequence in the current approach proceeds by calculating a new value of y^+ using the most recent value of a near-wall node tangential velocity and the appropriate wall function relations in a recursive manner. With y^+ evaluated, the appropriate value of the near-wall viscosity can be calculated. This value is then imposed at both the near-wall node and its nearest wall node to achieve a constant shear stress effect in the momentum equations. The boundary conditions (BCs) for k and ε are derived in terms of the wall shear stress using the near-wall assumption that production equals dissipation. These relations are given as follows:

k-BC

$$k_n = \frac{(\tau_w/\rho)^2}{C_\mu^{0\cdot 5}}, \tag{17}$$

ε-BC

$$\varepsilon_n = \frac{(\tau_W/\rho)^3}{\kappa y_n}. \tag{18}$$

The values obtained from these two expressions are applied at the near-wall node as boundary conditions. The wall nodes for the k-equation are specified to be zero and the wall nodes for the ε-equation are specified to be the most recent value of the nearest near-wall node value obtained from equation (18). As a result, there are effectively two consecutive rows or columns at all solid boundaries which provide the decoupling mechanism from the walls.

There are several unique capabilities in the current algorithm that were developed in order to implement the multiblock approach using a mixed-order formulation. The original design of the code always secured the minimal bandwidth for each flow model. This favourable characteristic was ensured by always numbering first in the direction with the fewest elements. The resulting logic used in the finite element model generator in this investigation was based on numbering both the corner and mid-side nodes in a sequential manner. The use of a frontal solver, such as the one proposed by

Hood,[20] requires that the corner nodes be numbered first, followed by the mid-side nodes. Such an approach will always require more in-core memory than necessary to solve the problem. In this work the desired minimum bandwidth attribute was maintained by implementing a new efficient method to solve and manipulate variables defined at only corner nodes with variables defined at all nodes. As an example, it is easy to visualize the indexing problem that occurs when a flow solver algorithm tries to solve for a velocity field with nodes numbered 1, 3, 5, etc. Flow solvers typically work more efficiently with a system of equations that are sequentially numbered from 1 to the total number of nodes.

Another unique aspect of the algorithm centres around the multiblock logic, as pertaining to the control logic of the bilinear variables. A new logic that implicitly derives the bilinear variable control indexing from the quadratic control parameters was developed. This feature greatly reduced the indexing problem by having a single set of parameters. The new logic was also designed to maintain the capability of the code to permit the exchange of information between blocks with faces which do not have the same number of elements. This method streamlines the memory usage, because only two grid blocks are in memory during any part of the solution update. This part of the algorithm reverts back to north, south, east and west finite volume orientation and assumes that all block are numbered in the direction which imposes a minimal bandwidth.

One unfavourable characteristic of the upwind scheme used in this is that it does not produce a positive definite matrix of influence coefficients. This prohibited the use of iterative solvers based on such strategies as that of the successive overrelaxation[21] or the conjugate gradient method with preconditioning.[22] The solver implemented was based on Gaussian elimination.[21] This solver was developed specifically to invert a global matrix stored in the format used by the current algorithm, as illustrated in Figure 1. This format stores only the bandwidth in memory, thus avoiding unnecessary multiplication by zeros.

3. RESULTS

The validation of the new multiblock algorithm using the RNG-based high-*Re* K–ε model is performed using data from a diffuser flow. This particular flow study was selected to show that the model is implemented correctly and to determine its performance relative to experimental data and the standard high-*Re* k–ε model.

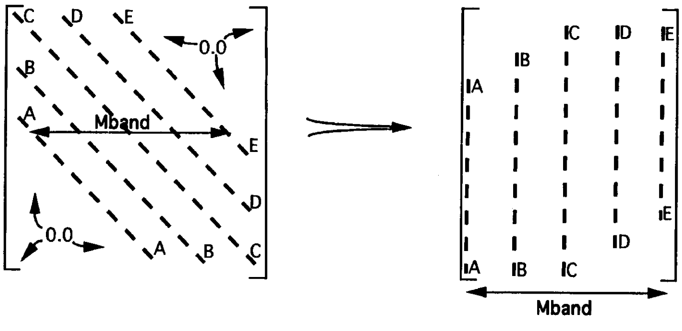

- Reduces incore memory requirements
- Accelerates the solvers

Figure 1. Storage method for global coefficient matrix (banded sparse matric approach)

The flow problem is that of a conical diffuser that was experimentally investigated by Stieglmeier *et al.*[23] The foremost flow structure in this problem is a separation zone that occurs along the diffuser wall. Accurate prediction of the reattachment length, which characterizes the recirculation zone, is used as a meaningful measure of how well the turbulence model performs with problems that contain strong adverse pressure gradients. The inlet Reynolds number for this study, based on the hydraulic diameter, is 15,600. This value is low for the application range of the RNG-based high-*Re* k–ε model. The problem, from this standpoint, is therefore viewed as a 'worst'-case problem.

The conical diffuser geometry is shown in Figure 2, along with the boundary conditions that were enforced. The inlet axial velocity profile was obtained through digitizing the reported data and the radial velocity was set to zero. The inlet profiles of k and ε were assumed constant and their values determined using the Reynolds stress data. As for the exit region, the zero-streamwise gradient approximation was imposed for all field variables with the exception of pressure, which was set to zero as datum value. This boundary condition, together with the zero-streamwise-gradient constraint, results in the well-known zero-surface-traction boundary condition. Finally, the wall functions were implemented over all solid walls in the manner described earlier.

A grid dependence study was initially performed to establish the necessary resolution of the finite element model. The selected criterion that had to be satisfied was that the recirculation zone length and pressure field remain essentially unchanged with further model refinement. For the purpose of consistency the distance between wall and near-wall nodes was kept constant for all finite element models. This value was obtained by enforcing the first node away from the wall at the inlet plane to have a y^+-value of 100. Furthermore, the length/width ratio of the elements was kept below 10. Using these criteria and guidelines, the point of grid independence was determined to occur between the case where the finite element model had 4544 and 5893 points. A single block was used for each case and the finite element model for these two models is shown in Figures 3 and 4. The results obtained with these models are compared using the streakline traces shown in Figure 5. This figure shows that the recirculation zones have practically the same reattachment length, which is approximately 9·5%

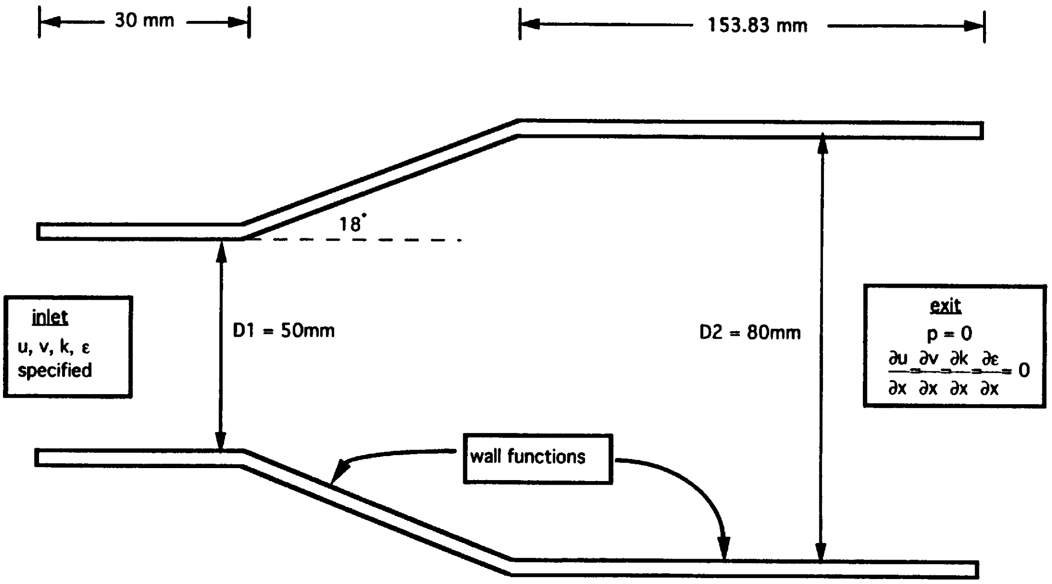

Figure 2. Conical diffuser geometry

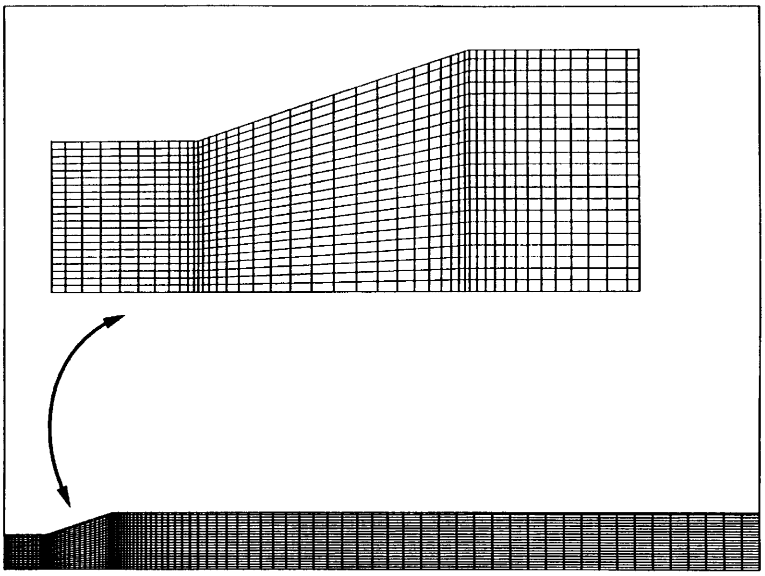

Figure 3. Finite element model using 4533 points

longer than the measured value. The pressure contours shown in Figure 6 show the same recovery characteristics. In addition, the turbulent viscosity distribution shown in Figure 7 is provided from the 5893-point case. This contour is actually the ratio of turbulent to laminar viscosity. As seen in the figure, this ratio is predicted not to exceed the value of 200.

The comparison of the current RNG-based high-*Re* k–ε model with the standard high-*Re* k–ε model was made using the conical diffuser finite element model shown in Figure 3. The streakline traces for

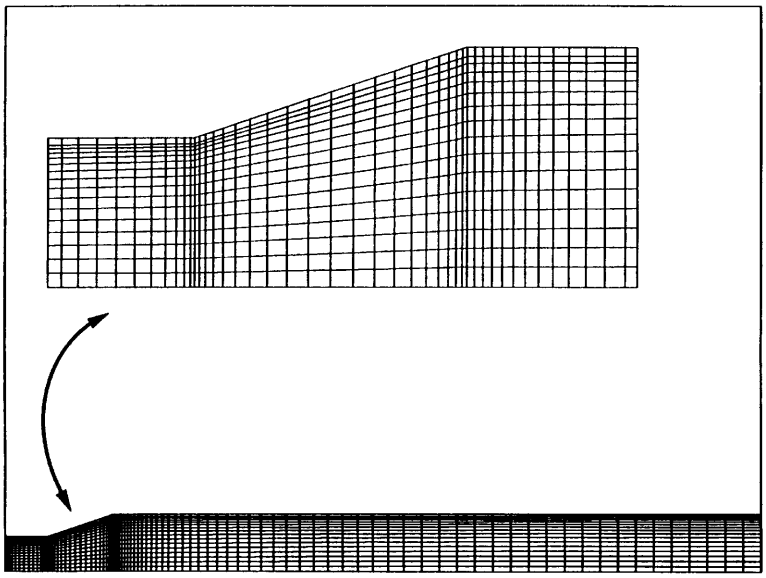

Figure 4. finite element model using 5893 points

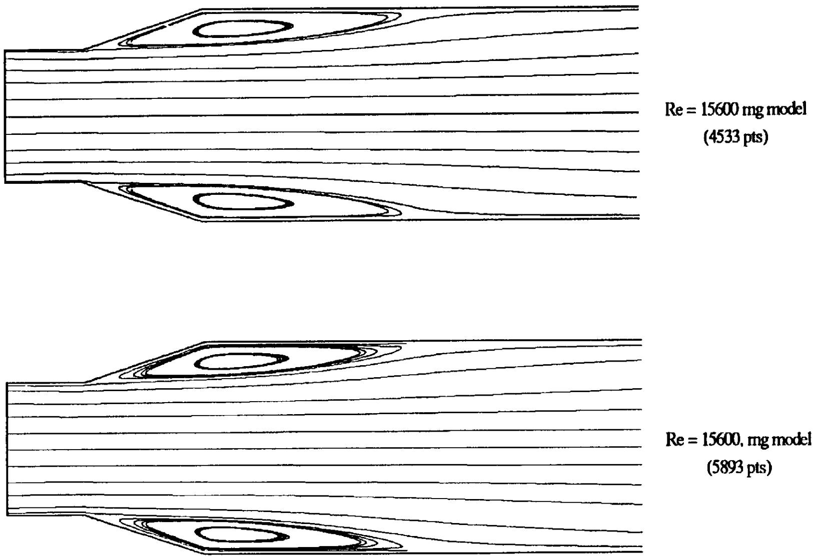

Figure 5. Comparison of streaklines to show grid independence

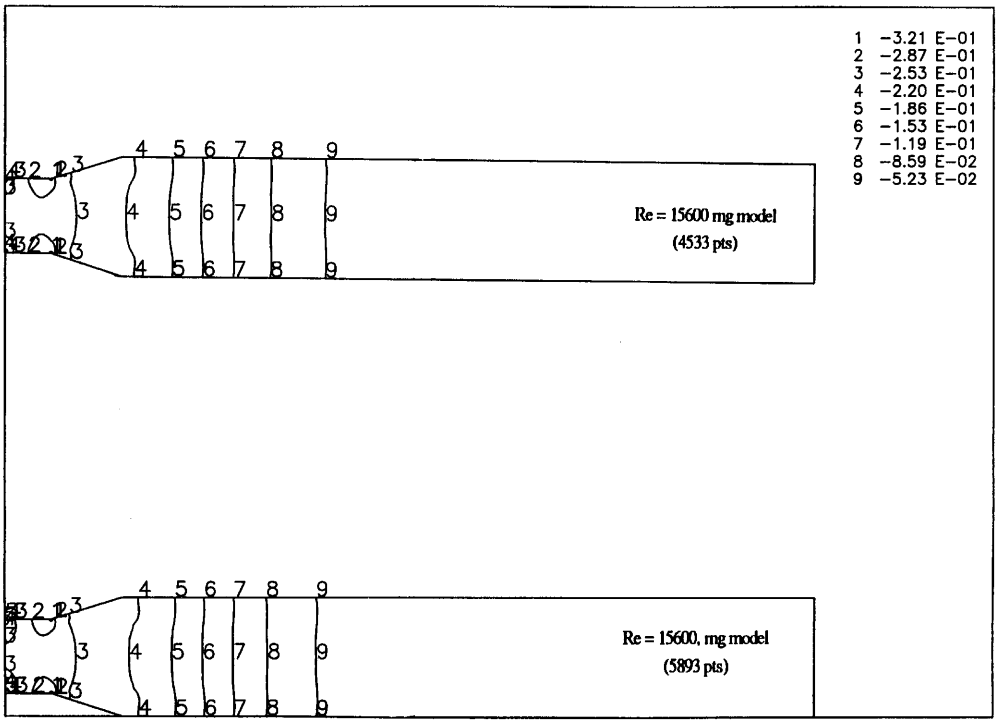

Figure 6. Comparison of pressure field characteristics

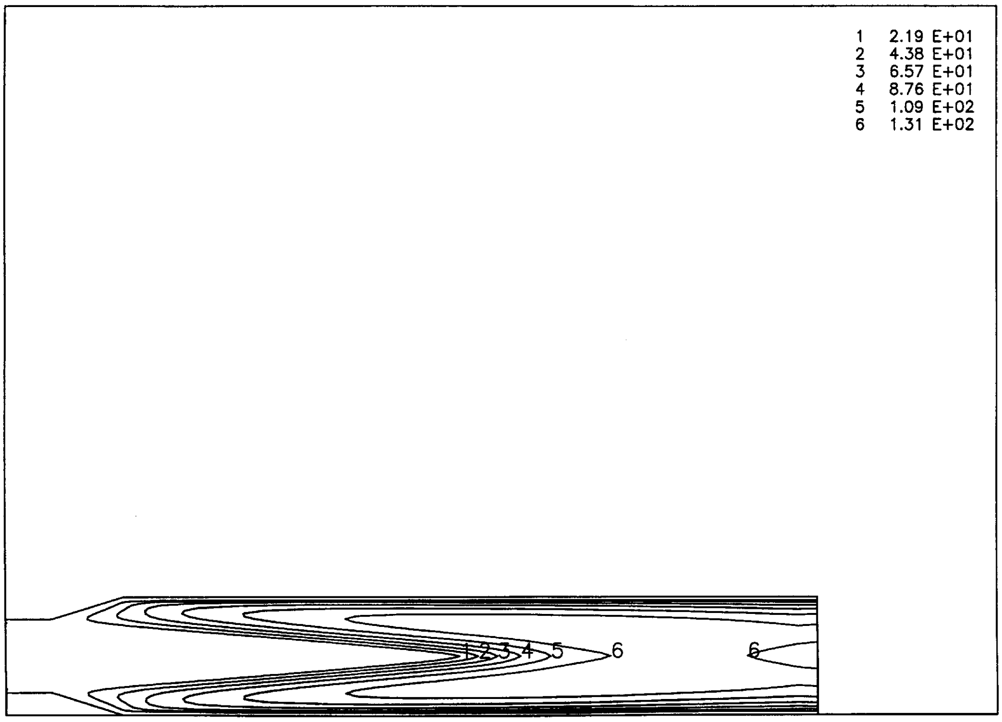

Figure 7. Turbulent viscosity ratio distribution

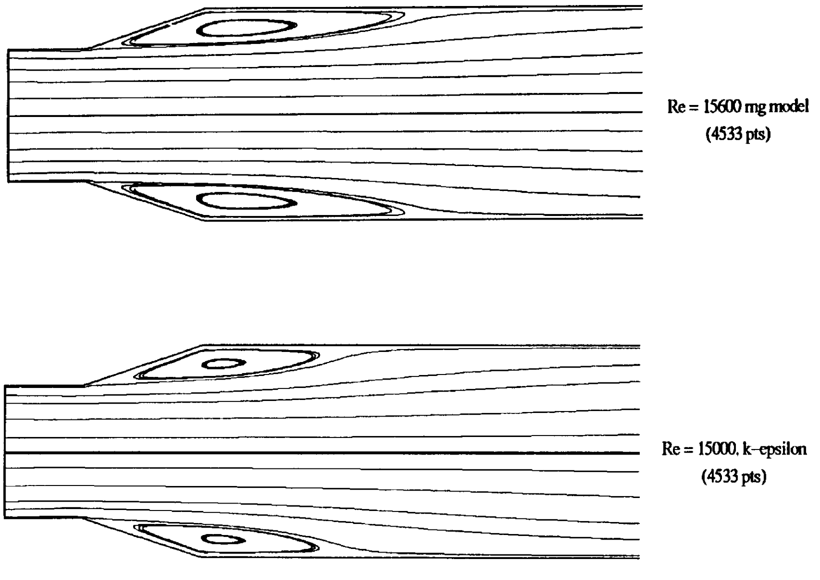

Figure 8. Streakline comparison between RNG model and standard k-ε model

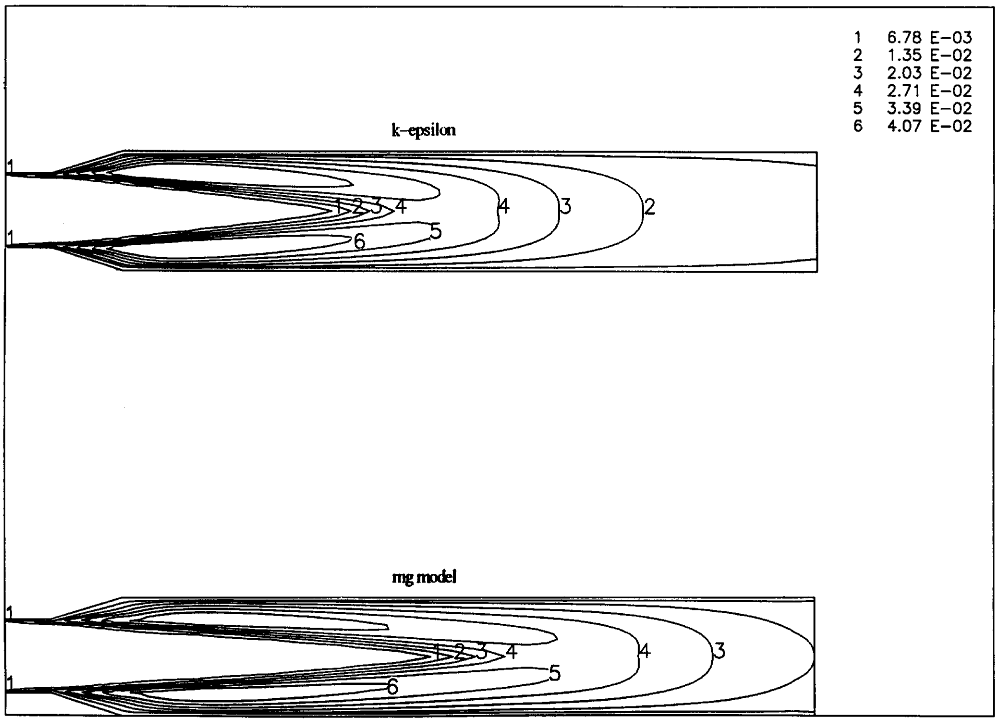

Figure 9. Comparison between turbulent kinetic energy profiles

these cases are compared in Figure 8. The shorter reattachment length predicted with the standard k–ε model shows this model's diffusive nature. This reattachment length was, comparatively, underpredicted by over 30%. The different characteristics between this model and the current RNG-based model can be further studied by comparing the turbulence kinetic energy distributions shown in Figure 9. Examination of this figure reveals that the turbulent kinetic energy distribution predicted by the high-*Re* k–ε model is more diffuse.

Development of the axial velocity profile is compared with the experimentally reported data in Figure 10. The predicted values in this figure reflect a realistic account of the flow field inside the conical diffuser. The slight overprediction of the recirculation zone length, detected in the figure, is attributed to the reported inlet swirl which was found to exist in the experimental rig.

The final study performed with this diffuser geometry was made to verify that the implementation of the new multiblock logic for the mixed-order formulation does not have an adverse effect on the numerical results. The finite element model created for this study is shown in Figure 11, along with the definition of the arbitrarily chosen four blocks. The resulting streakline traces are compared with the single-block case in Figure 12. This figure does not show any discontinuities across any interface boundaries, with reattachment lengths being identical for all practical purposes.

4. CONCLUSIONS

A complete study using a diffuser geometry was performed and reported. The first part of the study provided information on grid dependence for the finite element models and the second part demonstrated the characteristic differences between the current RNG-based high-*Re* k–ε model and

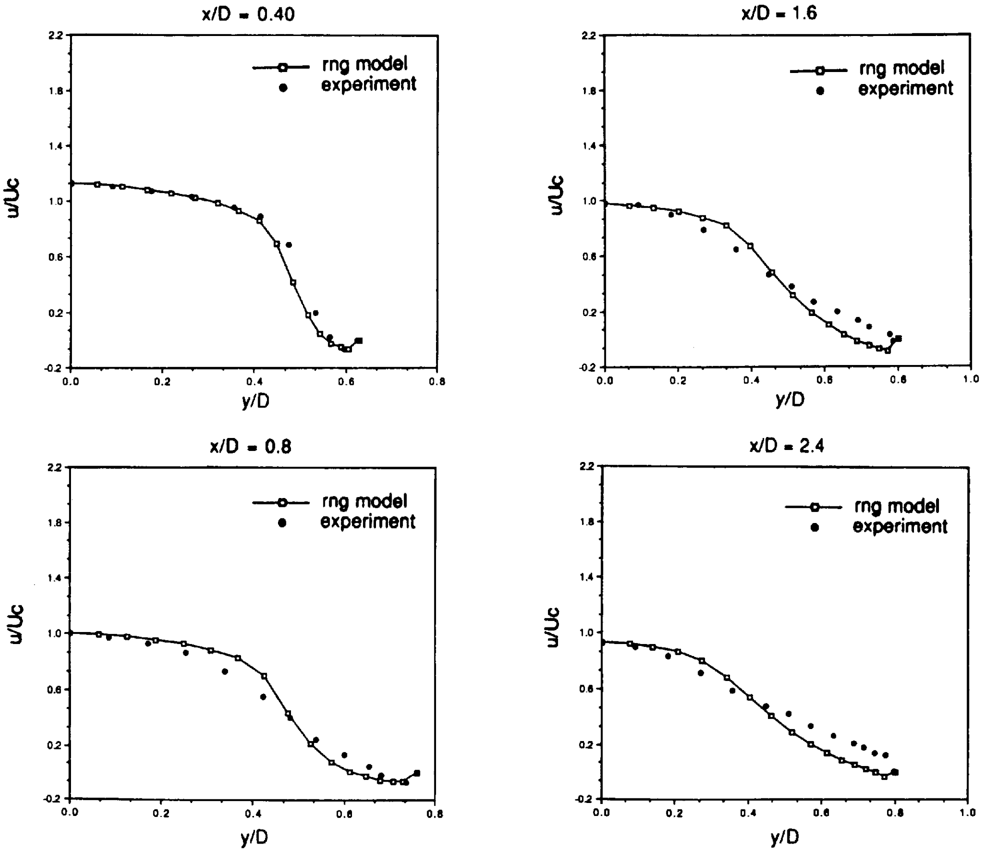

Figure 10. Comparison of axial velocity development with experimental data

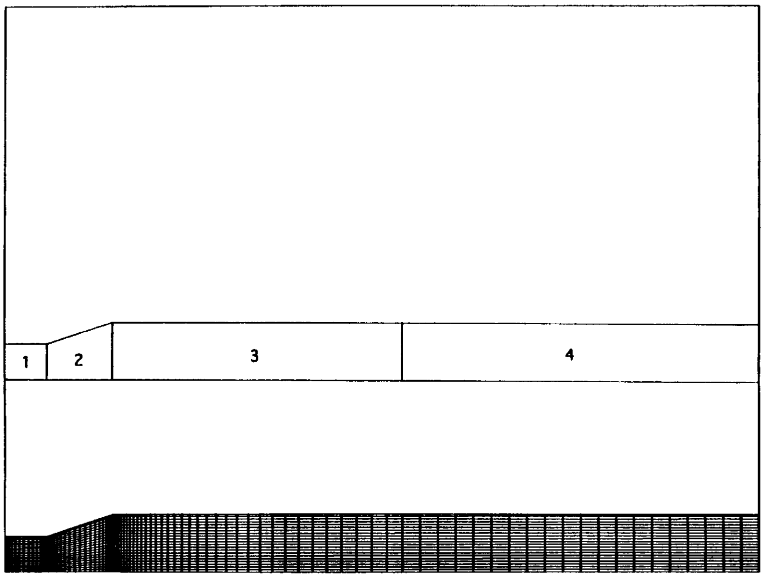

Figure 11. Finite element model and block definition

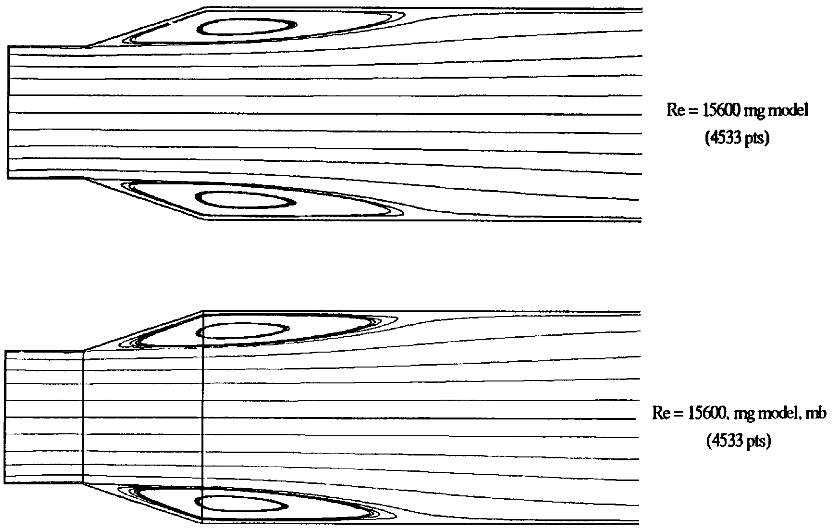

Figure 12. Comparison between multiblock and single-block cases using RNG model

the standard high-*Re* k–ε model for a flow domain with strong adverse pressure gradients. The standard high-*Re* k–ε model was shown to produce an overly diffuse flow field. This was detected in both the streakline traces and the turbulent kinetic energy contours. The last part of the study performed demonstrated that the new multiblock logic predicted the same values as the equivalent single-block case. Finally, the predicted results were compared with experimental data and were determined to slightly overpredict the reattachment length but yet provide a realistic flow field. This longer reattachment length was expected to be due to the reported effect of inlet swirl in the test rig.

ACKNOWLEDGEMENT

This study was funded by the Turbomachinery Research Consortium, contract 32519-15190.

REFERENCES

1. O. C. Zienkiewicz, *The Finite Element Method*, McGraw-Hill, London, 1977.
2. S. V. Patankar, *Numerical Heat Transfer and Fluid Flow*, Hemisphere, Washington DC, 1980.
3. J. G. Rice and R. J. Schnipke, 'An equal-order velocity–pressure formulation that does not exhibit spurious pressure modes', *Comput. Methods Appl. Mech. Eng.*, **57**, 135–149 (1986).
4. C. T. Shaw, 'Using a segregated finite element scheme to solve the incompressible Navier–Stokes equations', *Int. j numer. methods fluids*, **12**, 81–92 (1991).
5. G. Comini and S. Del Giudice, 'A (k–ε) model of turbulent flow', *Numer. Heat Transfer*, **8**, 133–147 (1985).
6. D. Hill and E. Baskharone, 'A multiblock Navier–Stokes algorithm using equal-order quadratic finite elements', *Int. j numer. methods fluids*, **20**, 169–185 (1995).
7. V. Yakhot, S. A. Orszag, S. Thangam T. B. Gatski and C. G. Speziale, 'Development of turbulence models for shear flows by a double expansion technique', *Phys. Fluids A*, **4**, 1510–1520 (1992).
8. A. G. Hutton, 'Progress in the development of a finite element wall model for high Reynolds number turbulent flow', *Appl. Math. Model.* **3** 322–326 (1979).
9. C. E. Thomas, K. Morgan and C. Taylor, 'A finite element analysis of flow over a backward facing step', *Comp. Fluids*, **9**, 265–278 (1981).
10. A. C. Benim and W. Zinser, 'Investigation into the finite element analysis of confined turbulent flows using a k–ε model of turbulence', *Comput. Methods in Appl. Mech. Eng.*, **51**, 507–523 (1985).
11. B. E. Launder and D. B. Spalding, 'The numerical computation of turbulent flows', *Comput. Methods Appl. Eng.*, **3**, 269–289 (1974).,

12. A. C. Benim, 'Finite element analysis of confined turbulent swirling flows', *Comput. Methods Appl. Mech. Eng.*, **11**, 697–717 (1990).
13. R. J. Schnipke, 'A streamline upwind finite element method for laminar and turbulent flow', *Ph.D. Dissertation*, University of Virginia, 1986.
14. *TEACH-2E*, Department of Mechanical Engineering, Imperial College, London, 1976.
15. *KIVA-II*, Los Alamos Laboratory, Los Alamos, NM, 1990.
16. W. M. Pun and D. B. Spalding, 'A general computer program for two-dimensional elliptic flows', *Rep. HTS/76/2*, Mechanical Engineering Department, Imperial College, London, 1976.
17. A. N. Brooks and T. J. R. Hughes, 'Streamline upwind/Petrov Glerkin formulation for convection dominated flows with particular emphasis on the incompressible Navier Stokes equations', *Comput. Methods Appl. Mech. Eng.*, **32** 199–259 (1982).
18. J. G. Rice and R. J. Schnipke, 'A monotone streamline upwind finite element method for convection-dominated flows', *Comput. Methods Appl. Mech. Eng.*, **47**, 313–327 (1984).
19. F. M. White, *Viscous Fluid Flow*, McGraw-Hill, New York, 1974.
20. P. Hood, 'Frontal solution program for unsymmetric matrices', *Int. j. numer. methods Eng.*, **10**, 379–399 (1976).
21. A. Ralston and P. Rabinowitz, *A Frst Course In Numerical Analysis*, McGraw-Hill, New York, 1979.
22. A. Freud and N. Nachtigal. 'QMR: a quasi-minimal residual meghod for non-Hermitian linear systems', *Numer. Math.*, **60**, 315–339 (1991).
23. M. Stieglmeier, C. Tropea, N. Weiser and W. Nitsche, Experimental investigation of the flow through axisymmetric expansions', *J. Fluids Eng.*, **111**, 464–469 (1989).